RSC Advances

ROYAL SOCIETY OF CHEMISTRY

www.rsc.org/advances

Facile synthesis of porous Fe_2TiO_5 microparticulates serving as anode material with enhanced electrochemical performances

Shimei Guo,[a,b] Shenyu Wang,[a] Nannan Wu,[a] Jiurong Liu,[a,*] Yuxing Ni,[c] and Wei Liu[c,*]

[a] Key Laboratory for Liquid–Solid Structural Evolution and Processing of Materials, Ministry of Education and School of Materials Science and Engineering, Shandong University, Shandong 250061, China

[b] College of Physics and Electronic Engineering, Qujing Normal University, Yunnan 655011, China

[c] State Key Laboratory of Crystal Materials, Shandong University, Shandong 250100, China

Abstract

Porous iron titanium oxide (Fe_2TiO_5) microparticulates have been successfully synthesized via a facile hydrothermal route followed by a subsequent calcination process. Polyvinyl-pyrrolidone (PVP), serving as a surfactant, played a pivotal role in controlling the size and inducing the mesoporous structure of Fe_2TiO_5. The measured specific surface area is 83.1 m^2 g^{-1} and the dominant pore size is ca. 10 nm. When tested as the anode material of lithium-ion batteries (LIBs), the as-prepared porous Fe_2TiO_5 microparticulates delivered a high reversible capacity of 468.3 mAh g^{-1} after 100 cycles at a current density of 100 mA g^{-1}, which nearly quadrupled that of porous TiO_2 microspheres and doubled that of Fe_2O_3 nanoparticles. Moreover, the porous Fe_2TiO_5 microparticulates also showed more superior rate capability and long-term cycling stability with respect to TiO_2 and Fe_2O_3 samples. Even after the rate performance test, a high discharge capacity of 234.1 mAh g^{-1} was still maintained at a current density of 500 mA g^{-1} over another 250 cycles. The improved electrochemical performances are mainly attributed to the synergistic effect of TiO_2 and Fe_2O_3 in Fe_2TiO_5, as well as the mesoporous structure.

Keywords: Fe_2TiO_5, cycling stability, rate capability, electrochemical performance

1. Introduction

In the past few decades, rechargeable lithium ion batteries (LIBs) have attracted remarkable attention due to their available high voltage, high energy density, no memory effect and long lifespan.[1-3] In general, the superior electrochemical performances of LIBs are largely dependent on their electrode materials, namely anode and cathode active material. Especially for anode active material, it has been playing an important role in determining energy density, safety and cycle life of LIBs.[4,5] Nowadays, the commercial anode material has been primarily dominated by graphite due to its beneficial layered structure for facile Li^+ insertion/extraction, good electrical conductivity, reasonable cost, and abundant resources. However, in the practical application, the potential for lithium insertion/extraction (0–0.25 V vs Li/Li^+) of graphite is close to that of the Li^+/Li redox couple, which will result in lithium plating and dendrite formation during the overcharge process, and thus generating serious safety issues (e.g., short out or explosion of LIBs).[6-8] In addition, graphite suffers greatly from volume expansion and shrinkage during Li-ion insertion and extraction that leads to the cracking of graphite particles and a loss in electrical contact, and thereby decreasing capacity as well as cycle life.[4] Especially, the low theoretical capacity (372 mAh g^{-1}) and poor cycling performance of graphite at high current density have restricted its large-scale application in high-power density batteries.[9] Recently, a lot of research attentions have been paid in seeking high capacity, high safety and long cycle-life anode materials to replace graphite.[10,11]

Among various prospective electrode materials, TiO_2 has been regarded as a very appealing anode candidate to compete with commercial graphite for LIBs owing to its superior structure stability, long cycle life, low cost and excellent security.[12-14] However, it is well known that TiO_2 possesses a relatively low theoretical capacity of 335 mAh g^{-1} even with the maximum

accommodation of one Li^+ per TiO_2 unit ($Li_{1.0}TiO_2$), poor rate capability due to its low electronic conductivity (~1×10^{-12} to 1×10^{-7} S cm^{-1}), and low lithium ion diffusivity (~1×10^{-15} to 1×10^{-9} cm^2 s^{-1}), which have seriously hindered its potential applications for commercialization.[15-17] To address the above issues, a series of Ti-based binary oxides with various of nanostructures, such as $SrTiO_3$ nanoparticles,[18] $FeTiO_3$ nanoflowers or nanosheets,[19,20] porous $TiNb_2O_7$ nanoparticles,[21] and $Zn_2Ti_3O_8$ nanowires,[22] have been synthesized as anode materials for LIBs. Benefited from the incorporation of high specific capacity from metal oxides (more than 335 mAh g^{-1}) and electrochemical stability of TiO_2, as well as the improved electronic conductivity and lithium ion diffusivity, these binary Ti-based oxide electrodes exhibited the enhanced reversible capacities and superior cycling performance. For example, the mesoporous $TiNb_2O_7$ nanocrystals as anode material for LIBs demonstrated a high capacity of 289 mA h g^{-1} (at 0.1 C) and an excellent rate performance of 162 mA h g^{-1} at 20 C and 116 mA h g^{-1} at 50 C (= 19.35 A g^{-1}).[21] The Si^{4+} doped $NiTiO_3$ spherical nanoparticles (140–160 nm) serving as anode material maintained a constant capacity ca. 400 mAh g^{-1} at a current density of 0.4 mA cm^{-2} up to 25 cycles.[23] $FeTiO_3$ nanosheets displayed a stable discharge capacity of ca. 430 mAh g^{-1} up to 90 cycles at a current density of 100 mA g^{-1}.[20]

Inspired by the above researches, in this work, a binary Ti-based oxide of Fe_2TiO_5 porous microparticulates have been synthesized through a facile hydrothermal route followed by a calcination process. Combining the high theoretical specific capacity of Fe_2O_3 (~1005 mAh g^{-1}) with the advantages of TiO_2 (e.g., superior structure stability and long cycle life),[5,12] the as-prepared Fe_2TiO_5 porous microparticulates exhibited the improved electrochemical performance with respect to pure TiO_2, Fe_2O_3 and the above mentioned binary Ti-based oxides anodes.

2. Experimental

2.1. Materials

Tetrabutyl titanate (TBT, $Ti(OC_4H_9)_4$, 99.0%), N,N-Dimethylformamide (DMF, C_5H_9NO, 99.0%), isopropanol (IPA, C_3H_8O, 99.0%), Iron(III) acetylacetonate ($C_{15}H_{21}FeO_6$, 98.0%), and polyvinyl-pyrrolidone (PVP, (C6H9NO)n, MW 40,000) were purchased from Sinopharm Chemical Reagent Co., Ltd. Carbon black, Li foil and Celgard 2300 were provided by Hefei Kejing Material Technology Co., Ltd, China. Polyvinylidene fluoride (PVDF), $LiPF_6$ (dissolved in ethylene carbonate, dimethyl carbonate, and ethylene methyl carbonate with a volume ratio of 1: 1: 1) were purchased from Shenzhen Biyuan Technology Co., Ltd, China. All the chemicals are of analytical grade and were used as received without further purification.

2.2. Preparation of Fe_2TiO_5 microparticulates

The preparation of porous Fe_2TiO_5 microparticulates is illustrated in Fig. 1. In a typical synthesis, 0.5 g polyvinyl-pyrrolidone (PVP) was firstly dissolved in the mixed organic solvent of 10 mL DMF and 30 mL IPA to form a transparent solution. Then, 1 mL TBT and 1 mmol Iron (III) acetylacetonate were added to the above solution under magnetic stirring until they were completely dissolved. The obtained bright red solution was transferred into a 65 mL Teflon-lined stainless steel autoclave, and subsequently sealed and heated at 180 ºC for 20 h in an oven. After reaction, the reddish brown precipitate was centrifuged and washed using deionized water and ethanol for five times, and then dried in a vacuum oven at 60 ºC overnight. The Fe_2TiO_5 product was obtained by annealing the reddish brown precursor at 500 ºC for 2 h in air. As comparison, pure TiO_2 and Fe_2O_3 samples were also prepared in the same procedure only without Iron (III) acetylacetonate and PVP or without TBT addition, respectively.

2.3. Characterizations

The structure of the resultant products was determined by X-ray powder diffraction (XRD) on a

Rigaku D/Max-RC X-ray diffractometer with Ni filtered Cu K_α radiation (λ = 0.1542 nm, V = 40 kV, I = 50 mA) in the range of 10-80° at a scanning rate of 4° min^{-1}. The morphology and microstructure of samples were examined by using a JSM-6700F field emission scanning electron microscope (FE-SEM) at an accelerating voltage of 20 kV and electric current of 1.0×10^{-10} A, and a JEOL JEM-2100 high resolution transmission electron microscope (HR-TEM) operated at 200 kV. The element contents were examined by energy-dispersive X-ray spectroscopy (EDS) detector attached to the FE-SEM. The N_2 adsorption/desorption isotherms of porous products were measured at 77 K on a Quadrasorb-SI instrument. The specific surface area was calculated with the Brunauer-Emmett-Teller (BET) model and the pore size distribution was determined using the Barrett-Joyner-Halenda (BJH) method. The composition was determined by X-ray photoelectron spectroscopy (XPS) on a Kratos Analytical spectrometer, using Al Kα (hν = 1486.6 eV) radiation as the excitation source under the anode voltage of 12 kV and emission current of 10 mA.

2.4. Electrochemical measurements

To prepare the working electrode，the active material, carbon black, and polyvinylidene fluoride (PVDF) with a weight ratio of 7:2:1 were mixed in N-methyl-2-pyrrolidinone (NMP) to form a homogenous slurry, which was coated on a copper foil substrate, followed by drying in a vacuum oven at 120 ºC for 12 h. The typical loading amount of active materials is 1.5–2.0 mg cm^{-2}. The CR2025-type cells were assembled using Li foil as counter and reference electrode, Celgard 2300 as separator, and 1 M LiPF6 (dissolved in ethylene carbonate, dimethyl carbonate, and ethylene methyl carbonate with a volume ratio of 1:1:1) as the electrolyte. The assembly was performed in a glove-box filled with argon atmosphere. The performance of the cells was evaluated galvanostatically in the voltage range from 0.02 to 3 V at various current densities on a

LAND CT2001A battery test system. Cyclic voltammogram (CV) was obtained by a PARSTAT 2273 electrochemistry workstation at a scan rate of 0.3 mV s^{-1} and the potential vs. Li/Li^+ ranging from 0.01 to 3 V. Electrochemical impedance spectra were tested on the same instrument with AC signal amplitude of 10 mV in the frequency range from 100 kHz to 0.01 Hz. The data were adopted to draw Nyquist plots using real part Z′ as X-axis, and imaginary part Z″ as Y-axis.

3. Results and discussion

XRD measurement was carried out to investigate the crystal phase of the as-prepared product. As shown in Fig. 2a, no obvious diffraction peak is observed in the Fe_2TiO_5 precursor indicating that the as-prepared precursor is amorphous. After being annealed at 500 ºC for 2 h in air, all the identified peaks can be assigned to the orthorhombic pseudobrookite Fe_2TiO_5 (JCPDS no. 41-1432, a_0 = 9.797 Å, b_0 =9.981 Å, c_0 = 3.73 Å),[24] and no any peak of other phase is detected (Fig. 2b), suggesting that the precursor has been completely converted into pure Fe_2TiO_5 after annealing process.

To further characterize the composition of Fe_2TiO_5 product, x-ray photoelectron spectroscopy (XPS) measurement was performed to determine the elements, chemical bonding, and their corresponding valence state. From the survey scan spectrum (Fig. 3a), the peaks of Fe 2p, Ti 2p, O 1s and C 1s were detected indicating the existence of Fe, Ti, O and C elements in the as-prepared Fe_2TiO_5 product. The C 1s signal can be attributed to the carbon contamination due to the ambient exposure of sample, which is usually found in oxides and consistent with our previous research.[25] The deconvoluted O 1s peaks at 531.5 and 532 eV (Fig. 3b) are assigned to C-O and Fe-O-Ti, respectively, according to the electronegativity successive decrease of C, Fe, and Ti elements. For the Fe 2p spectrum, two distinct peaks were observed around the binding

energies of 725.2 and 711.9 eV (Fig. 3c), which are assigned to Fe 2p1/2 and Fe 2p3/2, respectively. The fingerprint shakeup satellite peak of Fe_2O_3 appears at ca. 719.9 eV, suggesting that the valence of Fe in product is Fe^{3+}.[26-28] In Fig. 3d, the Ti 2p double peaks centered at ca. 458.3 and 464.2 eV stem from Ti 2p3/2 and Ti 2p1/2, respectively. The splitting binding energy between Ti 2p1/2 and Ti 2p3/2 core levels is ca. 5.9 eV, indicating a normal state of Ti^{4+} in product.[29-31]

The low-magnification SEM image reveals that the synthesized Fe_2TiO_5 microparticulates with the size of ca. 200 nm are agglomerated together to form larger cluster and have rough surface (Fig. 4a). Combining with HR-TEM observation (Fig. 4b), it can be confirmed that the as-prepared Fe_2TiO_5 has a porous architecture comprised of numerous nano-grains (ca. 10 nm) and pores. From the higher resolution image (Fig. 4c), two sets of lattice fringe spacings of 0.44 and 0.33 nm (inset of Fig. 4c) correspond to the (210) and (111) plane of pseudobrookite Fe_2TiO_5 (JCPDS no. 41-1432), respectively, consistent with the previous reports.[24,32] In Fig. 4d, the energy-dispersive spectrum (EDS) of Fe_2TiO_5 also confirms the presence of Fe, O and Ti elements agreement with the above XPS analysis (Fig. 3a). As comparison, the SEM images of as-synthesized TiO_2 and Fe_2O_3 samples are shown in Fig. S1a and b (supporting information). TiO_2 exhibits the morphology of porous microspheres with the diameter of ca. 500–800 nm (Fig. S1a), while the synthesized Fe_2O_3 is nanoparticles with a narrow size distribution of about 100 nm (Fig. S1b).

To investigate the effect of PVP on the morphology and structure of resultant product, the control experiments were operated with different addition amount of PVP while the other experimental parameters were kept the same as those mentioned in the aforementioned typical synthesis. Without PVP addition, the synthesized Fe_2TiO_5 has a spherical morphology with large

size distribution (1–5 μm) (Fig. 5a). From the high magnification FE-SEM image (inset of Fig. 5a), it is observed that Fe_2TiO_5 microspheres have smooth surface and solid structure, and no pores are found at the surface or interior of these microspheres. After 0.2 g PVP is added in the reaction, the morphology remains unchanged, while the obtained microspheres have a more narrow size distribution (less than 1μm) as shown in Fig. 5b. The high magnification FE-SEM image (inset of Fig. 5b) indicates the as-prepared Fe_2TiO_5 microsphere has a compact structure, and no obvious pores are observed except that the microsphere surface tends to rough. When the content of PVP increases to 0.5 g, the formed Fe_2TiO_5 microparticulates exhibit a porous structure and smaller size (Fig. 3). The spherical morphology disappeared due to the agglomeration among particles. With increasing the content of PVP to 1.0 g, the solution becomes very viscous, and the reddish brown precipitate of precursor cannot be obtained any more. Thus, PVP is believed to play an important role in controlling the morphology and size distribution and inducing the pore structure of Fe_2TiO_5 product. As a kind of nonionic surfactant, PVP can physically absorb on the surface of product subunits to prohibit the grain growth leading to a narrow size distribution.[33,34] In addition, due to the steric effect of PVP molecules, the grains are loosely aggregated to form larger particles. After annealed at 500 ºC in air, PVP molecules are oxidized into volatile CO_2 and H_2O, which are released to generate many voids in the interior as well as at surface of Fe_2TiO_5 microparticulates (Fig. 1).[35]

Porous structure can facilitate an efficient contact of the internal active materials with electrolyte, leading to a fast diffusion of Li^+ ions. Meanwhile, the high specific surface area and porosity are able to favorably alleviate the volume variation during the Li^+ insertion/extraction, resulting in a relatively high reversible capacity and cycling stability.[36,37] Therefore, nitrogen absorption-desorption measurements were performed to investigate the porosity and surface area

of Fe_2TiO_5 microparticulates and pure TiO_2 porous microspheres. As shown in Fig. 6a and 6b, the nitrogen adsorption/desorption isotherms of both samples exhibit a type IV nitrogen adsorption branch with a type-H3 hysteresis loop over the pressure range above 0.45 P/P_0, indicating the presence of mesopores in Fe_2TiO_5 microparticulates and TiO_2 microspheres.[8,9,37,38] From the pore size distribution curve of Fe_2TiO_5 microparticulates (inset of Fig. 6a), the pores with a size of ca. 10 nm are dominant consistent with the HR-TEM observation (Fig. 4b), and TiO_2 microspheres also exhibit similar pore size distribution (inset of Fig. 6b). The BET surface area of Fe_2TiO_5 porous microparticulates is 83.1 $m^2 g^{-1}$ and the pore volume is calculated to be 0.23 $cm^3 g^{-1}$, which are both higher than the corresponding values of 58.4 $m^2 g^{-1}$ and 0.14 $cm^3 g^{-1}$ for TiO_2 microspheres. The high specific surface area and pore volume are beneficial to the enhancement of cycling and rate performances of Fe_2TiO_5 microparticulates anode.

To reveal the electrochemical reaction of the as-synthesized Fe_2TiO_5 porous microparticulates as LIBs anode, cyclic voltammetry (CV) was carried out at room temperature in the range of 0.01–3.0 V at a scan rate of 0.3 mV s^{-1}. Li metal was used as the counter and reference electrodes. For comparison, pure TiO_2 porous microspheres and Fe_2O_3 nannoparticles were also employed as anode materials. The CV curves of TiO_2 porous microspheres (Fig. 7a) and Fe_2O_3 nannoparticles (Fig. 7b) are in good agreement with those of previously reported antase TiO_2 and α-Fe_2O_3.[16,38-40] However, it is worth noting that both of these two materials show a large decrease of cathodic current in the second CV curve with respect to the first one, suggesting the irreversible lithium insertion/extraction reaction and a large capacity loss during the initial two cycles.[13] On the contrary, the CV curves of Fe_2TiO_5 porous microparticulates (Fig. 7c) exhibit minor shrink during the initial two cycles comparing with the TiO_2 and Fe_2O_3 samples indicating its better reversibility. As shown in Fig. 7c, during the first discharge process, there are four clear

cathodic peaks observed at ca. 1.8, 1.7, 1.2 and 0.6 V, respectively. According to the reaction mechanism of TiO_2, Fe_2O_3 and previous researches of other multi-component oxides, the two conterminal irreversible peaks centered at ca. 1.8 V and 1.7 V, which disappear in the second cycle, can be attributed to the insertion of Li^+ into Fe_2TiO_5 resulting in the crystal structure destruction, and the lithium storage in TiO_2 to form Li_xTiO_2 ($TiO_2 + xLi^+ + xe^- \rightarrow Li_xTiO_2$).[10,16,41] The following peak at ca. 1.2 V corresponds to the lithium intercalation into Fe_2O_3 ($Fe_2O_3 + 2Li^+ + 2e^- \rightarrow Li(Fe_2O_3)$),[10,42,43] while the peak centered at about 0.6 V could be ascribed to the further reduction of Fe^{3+} into Fe^0 ($Li(Fe_2O_3) + 4Li^+ + 4e^- \rightarrow 2Fe^0 + 3Li_2O$), and the formation of amorphous Li_2O and solid–electrolyte interface (SEI) layer.[10,39,40] In the subsequent charge process, only one broad anodic peak from 1.5 V to 2.5 V (centered at about 2.1 V) is observed, which can be assigned to the oxidation of Fe^0 to Fe^{2+} and further oxidation to Fe^{+3} ($Fe^0 \rightarrow Fe^{2+}$ at ca. 1.6 V and $Fe^{2+} \rightarrow Fe^{3+}$ at ca. 1.9 V), as well as the extraction of Li ions from Li_xTiO_2 (at ca. 2.1V).[42,43] After the first cycle, the cathodic peaks at ca.1.8 V, 1.7 V and 1.2 V are replaced by a broad cathodic peak ranged from 1.1 V to 1.8 V in the subsequent cycles. The sharp cathodic peak at ca. 0.6 V in the first cathodic profile disappeared and only a weak shoulder peak was observed at ca. 0.5 V in the subsequent cycles, indicated that the active material was polarized and the SEI film was formed in the first cycle, corresponding to the large initial irreversible capacity.[39,44] From the second cycle onward, the CV curves are nearly overlapped, demonstrating that the electrochemical reaction tends to be stable.[43,45] In addition, the electrochemical reactions are also confirmed in the discharge–charge voltage profiles of Fe_2TiO_5 porous microparticulates. As shown in Fig. 7d, three short potential plateaus appear at ca. 1.8 (I), 1.2 (II) and 0.6 V (III) in the first discharge curve and a slope from 1.5 V to 2.5 V is observed in the subsequent charge, consistent with the

above CV analysis. When the first cycle is completed, the cell exhibits the initial discharge and charge capacities of 940.2 and 506.9 mAh g^{-1}, respectively, corresponding to the initial coulombic efficiency (the ratio of charge capacity to discharge capacity) of 54%. The large capacity loss of the as-prepared sample in the first cycle can be attributed to some lithium insertion into irreversible sites, the inevitable formation of solid electrolyte interface (SEI) film and Li_2O, and the active material loss by the disconnection of electrical contact during Li insertion that have been found in most anode materials.[46,47]

The cycling and rate performances of the as-synthesized Fe_2TiO_5 porous microparticulates, TiO_2 porous microspheres and Fe_2O_3 nanopatricles (Fig. S1a and S1b, supporting information) are depicted in Fig. 8. As shown in Fig. 8a, the reversible capacity of Fe_2TiO_5 anode is found to be 468.3 mAh g^{-1} after 100 cycles at a current density of 100 mA g^{-1} and the coulombic efficiency remains more than 95% after the initial three cycles. In comparison, the first discharge capacity (279.6 mAh g^{-1}) of TiO_2 at the current density of 100 mA g^{-1} is much lower than that (940.2 mAh g^{-1}) of Fe_2TiO_5, and the capacity is maintained at a low value of ca. 126.5 mAh g^{-1} in the successive cycling until 100th cycle. For Fe_2O_3 nanopatricles, although Fe_2O_3 anode exhibits the highest initial discharge capacity of 1295.3 mAh g^{-1} among three samples, it suffers from severe capacity fading in the subsequent cycling and only maintains a reversible capacity of 224.1 mAh g^{-1} after 100 cycles, which is less than half of porous Fe_2TiO_5 microparticulates. From the rate capability shown in Fig. 8b, compared with TiO_2 and Fe_2O_3 anodes, the Fe_2TiO_5 one also exhibits the higher reversible capacities of 363.7, 286, 239.3, 172.6, and 117.5 mAh g^{-1} at the current density of 100, 200, 400, 800 and 1600 mA g^{-1}, respectively, indicating that Fe_2TiO_5 also has more superior rate capability than other two samples. The detailed rate capability data of TiO_2 and Fe_2O_3 samples are listed in Table S1 (supporting information). When

the current density was returned to 100 mA g^{-1}, the discharge capacities of TiO_2 and Fe_2TiO_5 samples approximately returned back to their initial values and maintained stable cycling performance, suggesting that the high current charge/discharge process did little to break down the integrity of the electrodes.[48,49] It is noted that, although the Fe_2O_3 electrode recovers its initial capacity at first when the current density is returned to 100 mA g^{-1}, the electrode undergoes a capacity fading from 50 to 80 cycles, and only achieves a stable reversible capacity of ca. 126 mAh g^{-1} finally. To further evaluate the applicability of porous Fe_2TiO_5 microparticulates as anode materials in LIBs, the long cycling performance has also been investigated at a higher current density of 500 mA g^{-1} after the rate performance test (100 cycles). As shown in Fig. 8c, a reversible capacity of 234 mAh g^{-1} was maintained without obvious capacity fading even after another 250 cycles. It is worth noting that, as shown in Fig. 8a and 8c, the reversible capacities of Fe_2TiO_5 and Fe_2O_3 electrodes both firstly decrease in the initial several cycles and then increase for the following cycles. This phenomenon is commonly found in both Fe-based transition metal oxides and other metal oxides.[45,50] It can be attributed to the gradual improvement of lithium ion accessibility and additional capacity storage contributed by an organic polymeric/gel-like layer formed at low potential.[10,45,50] In addition, the presence of Fe nanoparticles at Fe_2TiO_5 or Fe_2O_3 interface caused by some irreversible electrochemical reaction is also a possible reason. It can improve the conductivity of electrode and the reversibility reaction of active material resulting in the enhanced capacity.[10,51] The more superior cycling and rate performances of Fe_2TiO_5 than TiO_2 microspheres and Fe_2O_3 nanopatricles demonstrate that the binary Ti-based oxide (Fe_2TiO_5) anode significantly exhibits the improved electrochemical performance as expected due to the synergistic effect of superior electrochemical stability of TiO_2 and high capacity of Fe_2O_3. In addition, the reversible capacity of the as-prepared porous Fe_2TiO_5 microparticulates is also

higher than those of the reported Fe_2TiO_5 nanoparticles prepared by ball milling (55.8 mAh g^{-1} after 50 cycles at a current density of 36 mA g^{-1}) and hydrothermal process (151.3 mAh g^{-1} after 50 cycles at a current density of 36 mA g^{-1})[24] mainly attributing to the high specific surface area and porosity of Fe_2TiO_5 microparticulates, which facilitate the efficient contact of internal active materials with electrolyte and the diffusion of Li^+ ions, and alleviate the volume variation during the Li^+ insertion/extraction, resulting in a relatively high reversible capacity and cycling stability.[36,37] Moreover, comparing with other binary Ti-based oxide anodes, such as $FeTiO_3$ nanoflowers (ca. 200 mAh g^{-1} after 50 cycles at a current density of 50 mA g^{-1}),[19] $FeTiO_3$ nanosheets (ca. 430 mAh g^{-1} after 90 cycles at a current density of 100 mA g^{-1}),[20] and $TiNb_2O_7$ nanocrystals (ca. 289 mA h g^{-1} after 10 cycles at a current density of 38.7 mA g^{-1}),[21] the as-synthesized porous Fe_2TiO_5 microparticulates also exhibit higher reversible capacity and better long-term cycling performance even at high current density (500 mA g^{-1}), further confirming the superiority of the as-synthesized porous Fe_2TiO_5 microparticulates for LIBs anode.

To further clarify the electrochemical performance of Fe_2TiO_5 anode, electrochemical impedance spectroscopy (EIS) measurements were performed from 100 kHz to 0.01 Hz. Fig. 9 presents the Nyquist plots of Fe_2TiO_5 porous microparticulates, TiO_2 porous microspheres and Fe_2O_3 nanoparticles after 100 charge/discharge cycles at a current density of 100 mA g^{-1}. The EIS data are analyzed by fitting to an equivalent electrical circuit shown in the inset of Fig. 9, in accordance with the Li-ion insertion/extraction mechanism in electrode.[2,13,52] As can be seen in Fig. 9, the Nyquist plots of Fe_2TiO_5 and TiO_2 are both comprised of a depressed semicircle in the high- and medium-frequency region and an inclined line in the low frequency region, while Fe_2O_3 sample displays two arcs in the high- and medium-frequency region and a short linear tail in the low frequency. The diameter of semicircle in high- and medium-frequency region of each

cell is related to the electrolyte resistance (R_e), the SEI resistance (R_{sf}) and the charge transfer resistance (R_{ct}), while the inclined line in low frequency region represents the Warburg impedance (Z_w) that is derived from the lithium ion diffusion in electrode materials.[10,43] Obviously, the diameter of semicircle for Fe_2TiO_5 sample (ca.142 Ω) is much smaller than that of TiO_2 (ca. 322 Ω), indicating a lower internal resistance of Fe_2TiO_5. Comparing with Fe_2O_3 nanoparticles, the Fe_2TiO_5 anode also displays a smaller internal resistance (R_e+R_{sf} +R_{ct}) as listed in Table S2 (supporting information), suggesting more efficient transfer of electrons and Li ions between the interface of Fe_2TiO_5 microparticulates and electrolyte, which is beneficial to the capacity enhancement of Fe_2TiO_5 anode. In addition, the largest slope of inclined line in low frequency region for Fe_2TiO_5 anode demonstrates faster diffusion of Li ions in Fe_2TiO_5 than in TiO_2 and Fe_2O_3 samples due to the porous structure with higher specific surface area and larger pore volume (Fig. 4 and 6), which improves the diffusion of electrolyte and the interfacial contact between active material and electrolyte and shortens the lithium diffusion path.[33,36] Therefore, the lower internal resistance and faster diffusion rate of lithium ions in Fe_2TiO_5 porous microparticulates than in TiO_2 and Fe_2O_3 samples might be the main reasons for the enhanced cycling performance and rate capability of Fe_2TiO_5 anode.

4. Conclusions

In summary, porous Fe_2TiO_5 microparticulates have been synthesized as anode material for Li-ion battery by a facile approach, in which PVP is a key factor in controlling the particle size and inducing the pore structure of Fe_2TiO_5. Comparing with the as-prepared TiO_2 porous microspheres and Fe_2O_3 nanoparticles, porous Fe_2TiO_5 microparticulates exhibited much higher reversible capacity and superior long-term cycling performance even at high current density due to the combination of electrochemical stability of TiO_2 and high capacity of Fe_2O_3. The

experimental results confirm that the porous Fe_2TiO_5 microparticulates have lower internal resistance and faster diffusion rate of lithium ions than TiO_2 and Fe_2O_3 samples, which are also beneficial to enhance the cycling performance and rate capability of Fe_2TiO_5 anode.

Acknowledgements

This work was supported by the Fundamental Research Funds of Shandong University (2015JC016, 2015JC036) and the National Natural Science Foundation of China (No. 51572157). The authors also acknowledge the financial supports from the Science and Technology Development Plan (2014GGX102004) and Natural Science Fund for Distinguished Young Scholars of Shandong (JQ201312).

References

1 Q. Wang, Z. Wen and J. Li, *Adv. Funct. Mater.*, 2006**, 16**, 2141-2146.

2 Y. Wang, M. Wu and W. F. Zhang, *Electrochim. Acta*, 2008**, 53**, 7863-7868.

3 Y. Guo, J. Hu and L. Wan, *Adv. Mater.*, 2008**, 20**, 2878-2887.

4 G. Zhu, Y. Wang and Y. Xia, *Energ. Environ. Sci.*, 2012**, 5**, 6652-6667.

5 Y. Luo, J. Luo, J. Jiang, W. Zhou, H. Yang, X. Qi, H. Zhang, H. J. Fan, D. Y. W. Yu, C. M. Li and T. Yu, *Energ. Environ. Sci.*, 2012**, 5**, 6559-6566.

6 F. Wu, X. Li, Z. Wang and H. Guo, *Nanoscale*, 2013**, 5**, 6936-6943.

7 W. Li, F. Wang, Y. Liu, J. Wang, J. Yang, L. Zhang, A. A. Elzatahry, D. Al-Dahyan, Y. Xia and D. Zhao, *Nano Lett.*, 2015**, 15**, 2186-2193.

8 V. Etacheri, Y. Kuo, A. Van der Ven and B. M. Bartlett, *J. Mater. Chem. A*, 2013**, 1**, 12028-12032.

9 X. Li, Y. Zhang, T. Li, Q. Zhong, H. Li and J. Huang, *J. Power Sources*, 2014**, 268**, 372-378.

10 J. Luo, X. Xia, Y. Luo, C. Guan, J. Liu, X. Qi, C. F. Ng, T. Yu, H. Zhang and H. J. Fan, *Adv. Energy Mater.*, 2013**, 3**, 737-743.

11 Y. Luo, J. Luo, W. Zhou, X. Qi, H. Zhang, D. Y. W. Yu, C. M. Li, H. J. Fan and T. Yu, *J. Mater. Chem. A*, 2013**, 1**, 273-281.

12 L. Xin, Y. Liu, B. Li, X. Zhou, H. Shen, W. Zhao and C. Liang, *Sci. Rep.*, 2014**, 4**, 4479-4485.

13 Z. Wen, S. Ci, S. Mao, S. Cui, Z. He and J. Chen, *Nanoscale Res. Lett.*, 2013**, 8**, 499-504.

14 H. Wang, D. Ma, X. Huang, Y. Huang and X. Zhang, *Sci. Rep.*, 2012**, 2**, 701-708.

15 X. Li, Y. Chen, H. Yao, X. Zhou, J. Yang, H. Huang, Y. Mai and L. Zhou, *RSC Adv.*, 2014**, 4**, 39906-39911.

16 W. Luo, X. Hu, Y. Sun and Y. Huang, *J. Mater. Chem.*, 2012**, 22**, 4910-4915.

17 B. Li, Q. Zhang, C. Zhang, S. Kang, X. Li and Y. Wang, *Int. J. Electrochem. Sc.*, 2013**, 8**, 8414-8421.

18 D. C. Johnson and A. L. Prieto, *J. Power Sources*, 2011**, 196**, 7736-7741.

19 T. Tao, A. M. Glushenkov, M. M. Rahman and Y. Chen, *Electrochim. Acta*, 2013**, 108**, 127-134.

20 X. Guan, J. Zheng, M. Zhao, L. Li and G. Li, *RSC Adv.*, 2013**, 3**, 13635-13641.

21 C. Jo, Y. Kim, J. Hwang, J. Shim, J. Chun and J. Lee, *Chem. Mater.*, 2014**, 26**, 3508-3514.

22 Z. Hong, M. Wei, Q. Deng, X. Ding, L. Jiang and K. Wei, *Chem. Commun.*, 2010**, 46**, 740-742.

23 V. D. Nithya, R. K. Selvan, K. Karthikeyan and Y. S. Lee, *J. Nanosci. Nanotechno.*, 2015**, 15**, 694-702.

24 K. Min, K. Park, A. Lim, J. Kim and D. Kim, *Ceram. Int.*, 2012**, 38**, 6009-6013.

25 J. Liu, Y. Mao, E. Lan, D. R. Banatao, G. J. Forse, J. Lu, H. Blom, T. O. Yeates, B. Dunn and J. P. Chang, *J. Am. Chem. Soc.*, 2008**, 130**, 16908-16913.

26 T. Fujii, F. de Groot, G. A. Sawatzky, F. C. Voogt, T. Hibma and K. Okada, *Phys. Rev. B*, 1999**, 59**, 3195-3202.

27 A. P. Grosvenor, B. A. Kobe, M. C. Biesinger and N. S. McIntyre, *Surf. Interface Anal.*, 2004**, 36**, 1564-1574.

28 J. Shao, J. Zhang, J. Jiang, G. Zhou and M. Qu, *Electrochim. Acta*, 2011**, 56**, 7005-7011.

29 Y. Wang, T. Chen and Q. Mu, *J. Mater. Chem.*, 2011**, 21**, 6006-6013.

30 Z. Ali, S. N. Cha, J. I. Sohn, I. Shakir, C. Yan, J. M. Kim and D. J. Kang, *J. Mater. Chem.*, 2012**, 22**, 17625-17629.

31 H. Xia, W. Xiong, C. K. Lim, Q. Yao, Y. Wang and J. Xie, *Nano Res.*, 2014**, 7**, 1797-1808.

32 M. Guo, J. Zhao, X. Xu, G. Liu and X. Wang, *Ceram. Int.*, 2014**, 40**, 5825-5830.

33 L. Li, Y. Cheah, Y. Ko, P. Teh, G. Wee, C. Wong, S. Peng and M. Srinivasan, *J. Mater. Chem. A*, 2013**, 1**, 10935-10941.

34 Y. Li, H. Zhang, X. Li, H. Zhang and W. Wei, *J. Power Sources*, 2013**, 233**, 202-208.

35 D. Wang, P. Yang and X. Cheng, *Nanosci. Nanotech. Let.*, 2015**, 7**, 358-364.

36 M. A. Rahman, Y. C. Wong, G. Song and C. Wen, *J. Porous Mat.*, 2015**, 22**, 1313-1343.

37 S. Guo, G. Lu, S. Qiu, J. Liu, X. Wang, C. He, H. Wei, X. Yan and Z. Guo, *Nano Energy*, 2014**, 9**, 41-49.

38 J. S. Chen, H. Liu, S. Z. Qiao and X. W. D. Lou, *J. Mater. Chem.*, 2011**, 21**, 5687-5692.

39 Y. Fu, Q. Wei, X. Wang, H. Shu, X. Yang and S. Sun, *J. Mater. Chem. A*, 2015**, 3**, 13807-13818.

40 J. S. Cho, Y. J. Hong and Y. C. Kang, *ACS Nano*, 2015**, 9**, 4026-4035.

41 F. Lin, H. Song, S. Tian, X. Chen, J. Zhou and F. Wang, *Electrochim. Acta*, 2012**, 83**, 305-310.

42 J. Morales, L. Sanchez, F. Martin, F. Berry and X. L. Ren, *J. Electrochem. Soc.*, 2005**, 152**, A1748-A1754.

43 M. V. Reddy, T. Yu, C. Sow, Z. X. Shen, C. T. Lim, G. V. S. Rao and B. V. R. Chowdari, *Adv. Funct. Mater.*, 2007**, 17**, 2792-2799.

44 Z. Xiao, C. Haoxin, X. Yaping and G. Jinxue, *J. Mater. Chem. A*, 2014**, 2**, 3912-3918.

45 L. Gao, H. Hu, G. Li, Q. Zhu and Y. Yu, *Nanoscale*, 2014**, 6**, 6463-6467.

46 S. Kim, K. Kim, S. Lee, S. Kim, J. S. Kim and J. K. Lee, *Curr. Appl. Phys.*, 2013**, 13**, 1923-1927.

47 D. Yuan, W. Yang, J. Ni and L. Gao, *Electrochim. Acta*, 2015**, 163**, 57-63.

48 X. Gu, L. Chen, Z. Ju, H. Xu, J. Yang and Y. Qian, *Adv. Funct. Mater.*, 2013**, 23**, 4049-4056.

49 Y. Liu, X. Zhao, F. Li and D. Xia, *Electrochim. Acta*, 2011**, 56**, 6448-6452.

50 F. Wu, R. Huang, D. Mu, B. Wu and S. Chen, *ACS Appl. Mater. Inter.*, 2014**, 6**, 19254-19264.

51 L. Pan, X. Zhu, X. Xie and Y. Liu, *Adv. Funct. Mater.*, 2015**, 25**, 3341-3350.

52 W. Yue, S. Tao, J. Fu, Z. Gao and Y. Ren, *Carbon*, 2013**, 65**, 97-104.

Figures and captions

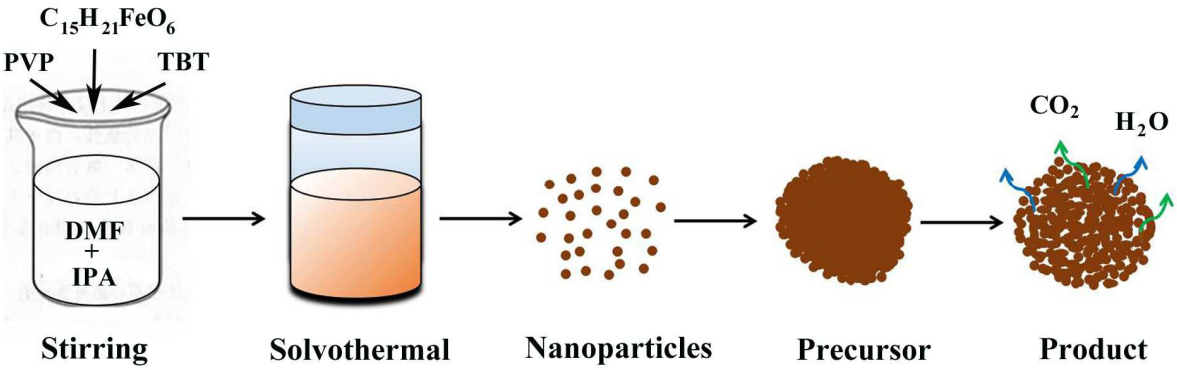

Fig. 1 Schematic illustration for the fabrication process of porous Fe_2TiO_5 microparticulates.

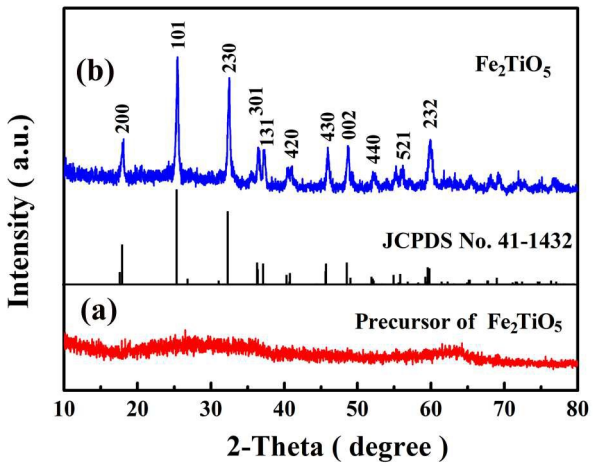

Fig. 2 XRD patterns of (a) Fe_2TiO_5 precursor and (b) Fe_2TiO_5 microparticulates.

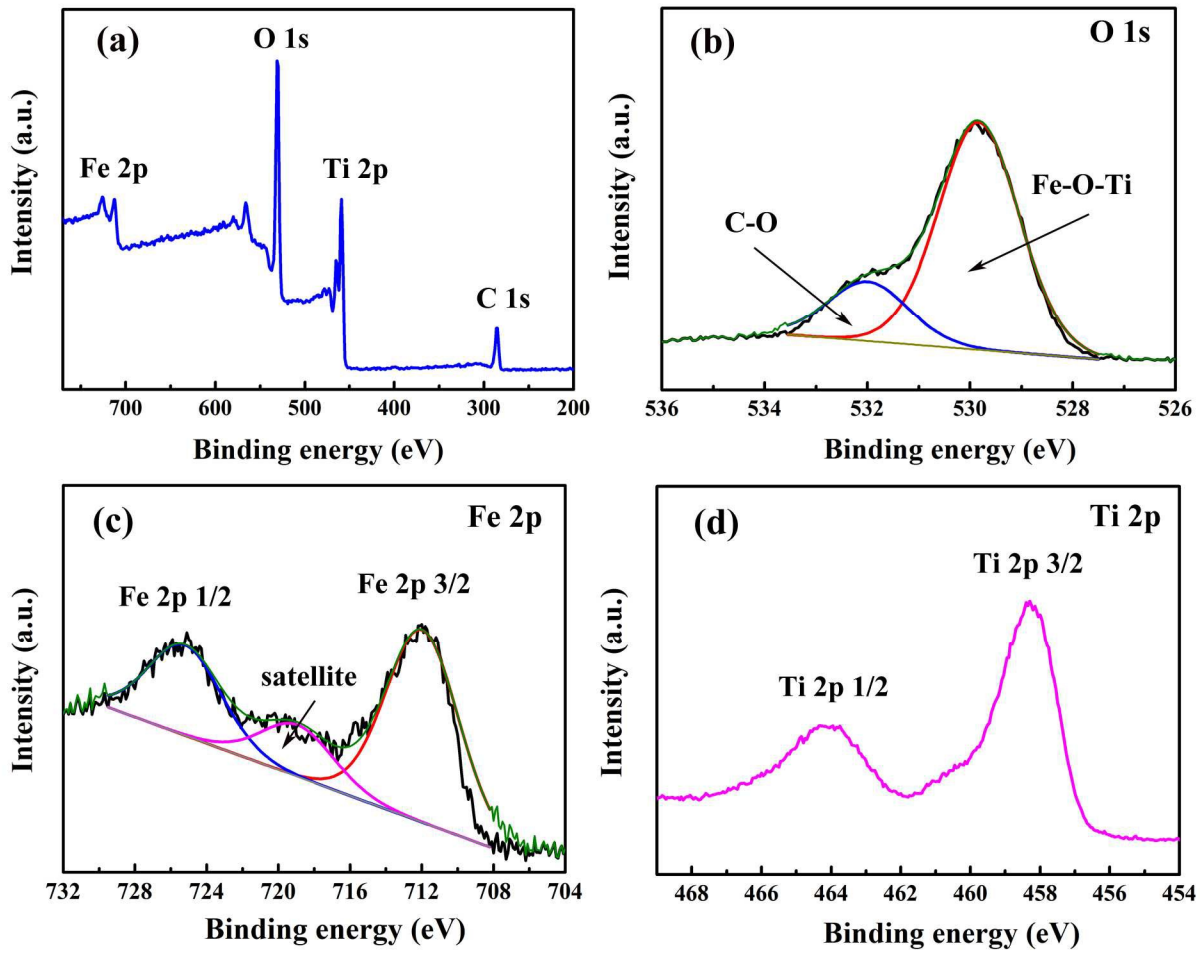

Fig. 3 XPS spectra of (a) survey scan, (b) O 1s, (c) Fe 2p and (d) Ti 2p of Fe_2TiO_5 microparticulates.

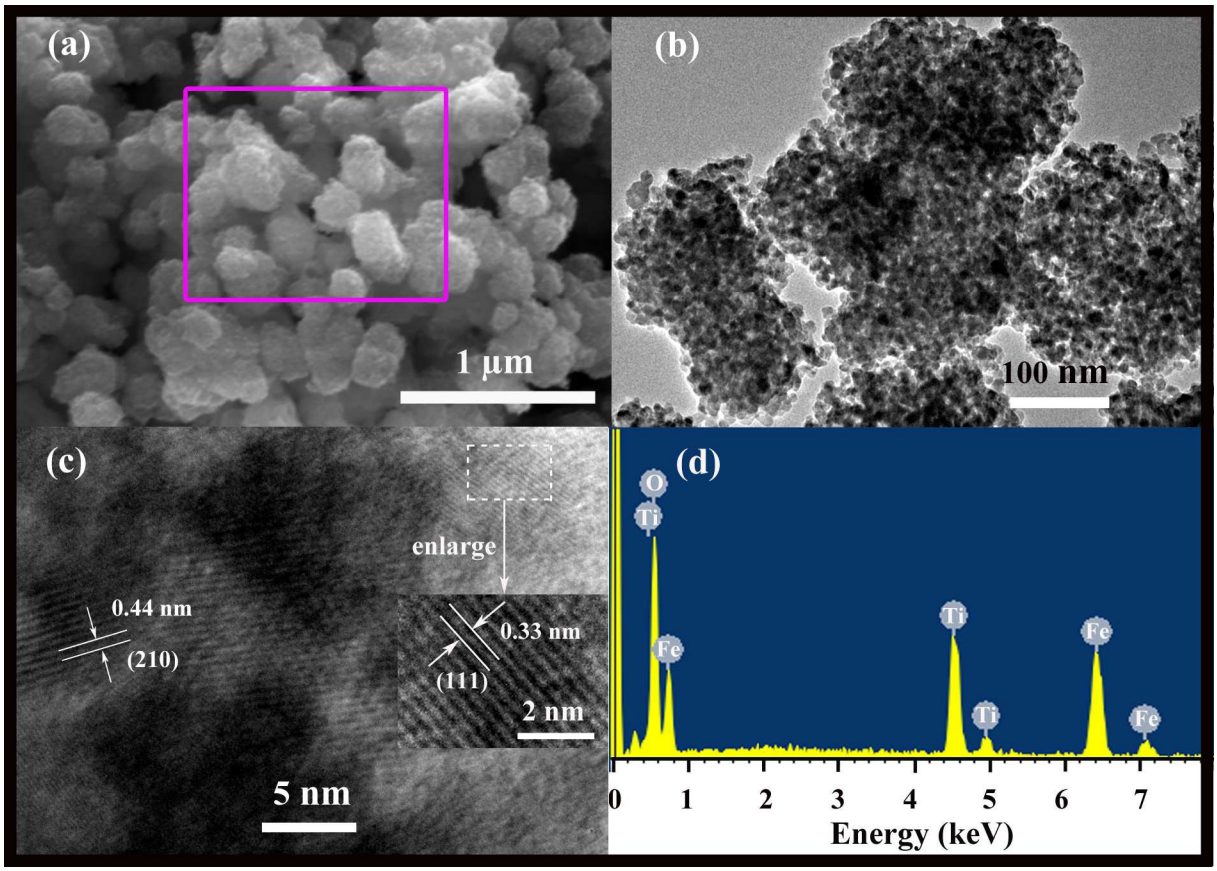

Fig. 4 SEM images (a), TEM images (b), HR-TEM images (c), and the corresponding EDS spectrum from the marked areas in (a) of as-prepared Fe_2TiO_5 microparticulates.

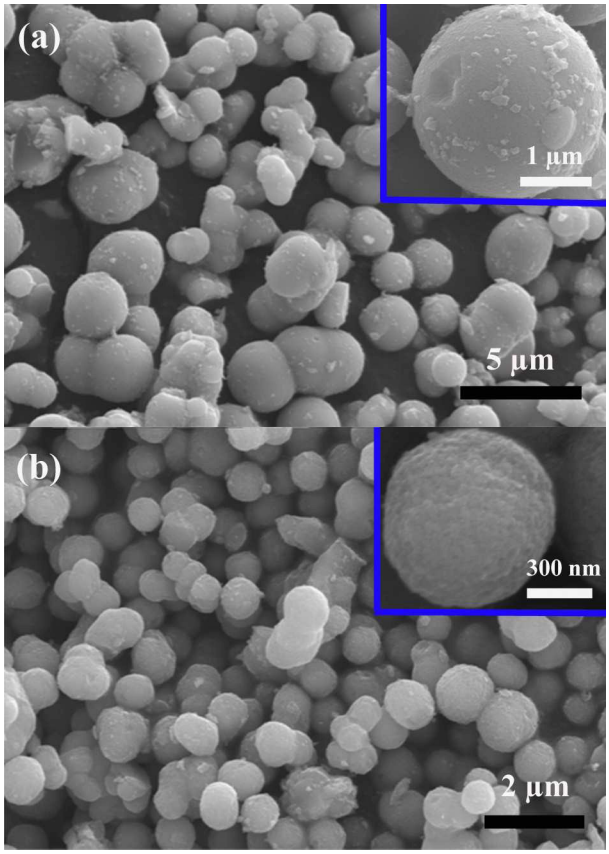

Fig. 5 FE-SEM images of Fe_2TiO_5 fabricated with different amount of PVP: (a) 0 g and (b) 0.2 g.

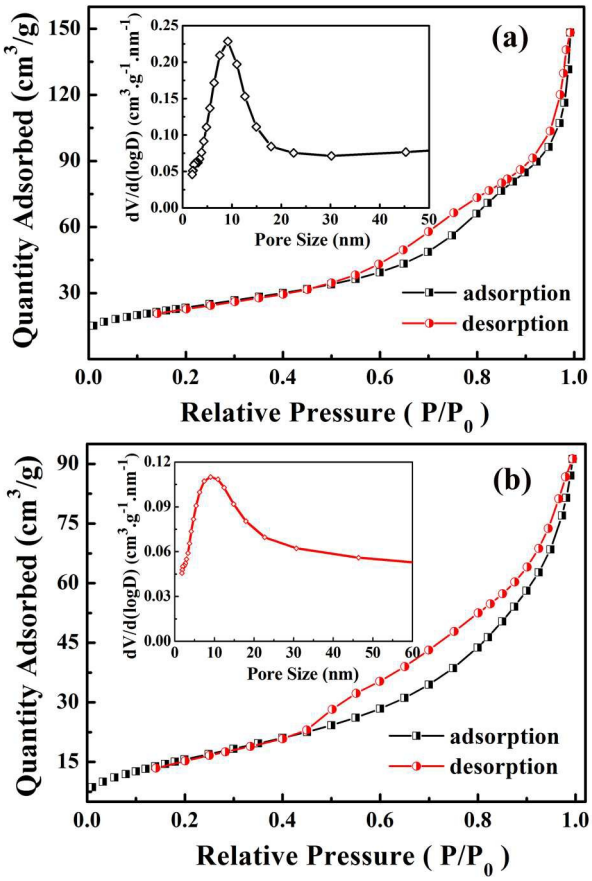

Fig. 6 N_2 adsorption-desorption isotherms of porous TiO_2 microspheres (a) and Fe_2TiO_5 microparticulates (b). The insets are pore size distribution curves.

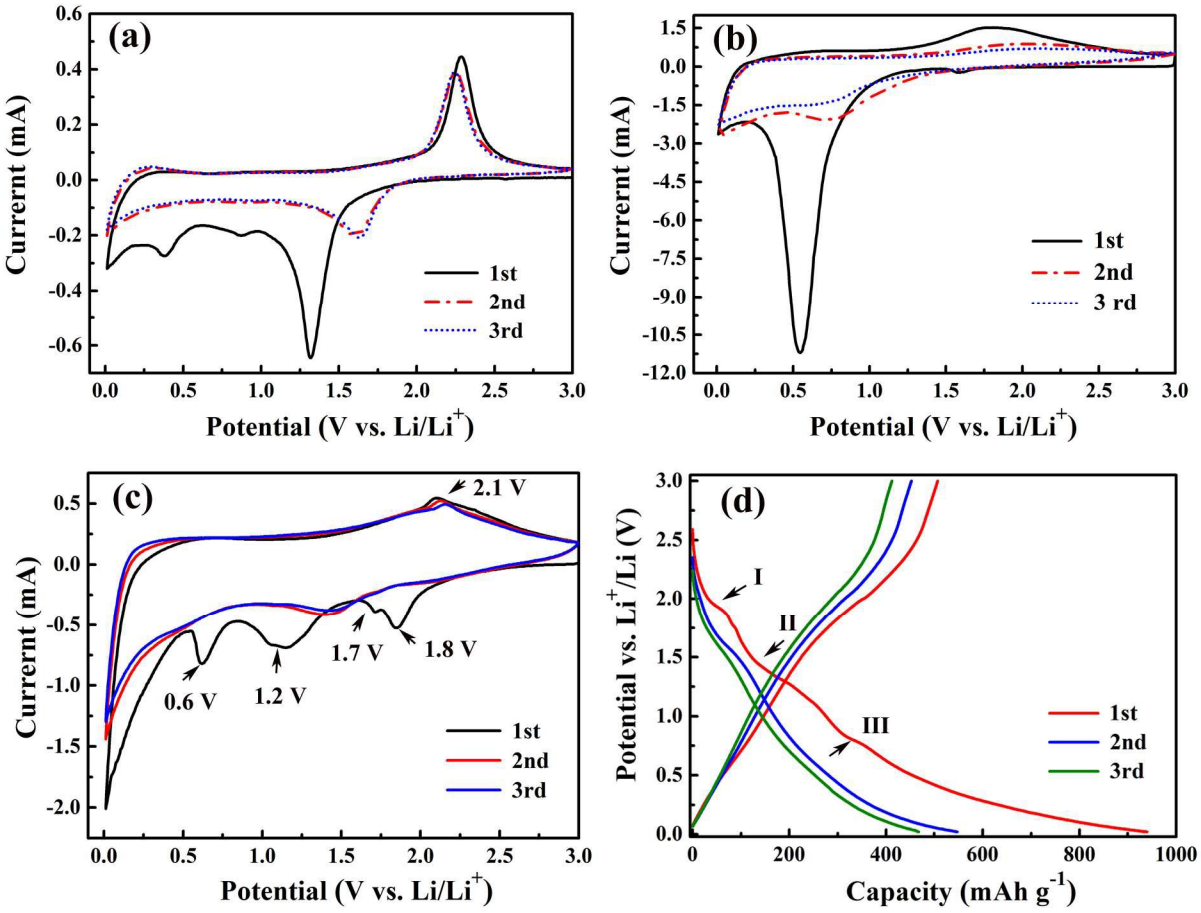

Fig. 7 Cyclic voltammetry (CV) curves of TiO_2 microspheres (a), Fe_2O_3 nanoparticles (b) and Fe_2TiO_5 microparticulates (c) at a scan rate of 0.3 mV s^{-1} in the range of 0.01–3.0 V. Galvanostatic discharge/charge curves of the initial three cycles for Fe_2TiO_5 microparticulates (d).

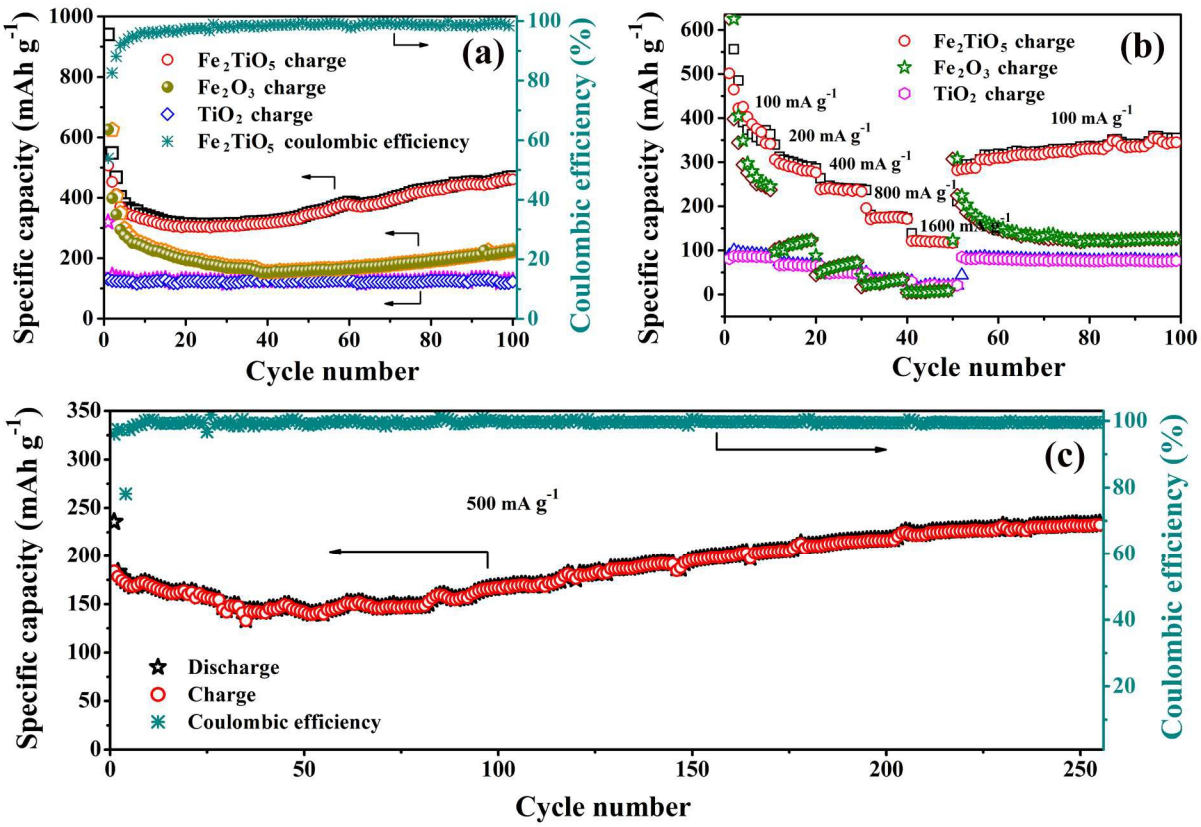

Fig. 8 (a) Cycling performances of TiO_2 microspheres, Fe_2O_3 nanoparticles and Fe_2TiO_5 microparticulates, and coulombic efficiency of Fe_2TiO_5 microparticulates at the current density of 100 mAh g^{-1}. (b) Rate capabilities of TiO_2, Fe_2O_3 and Fe_2TiO_5 at different cycling rates. (c) Long-term cycling performance of Fe_2TiO_5 microparticulates at the current density of 500 mA g^{-1} after rate performance test.

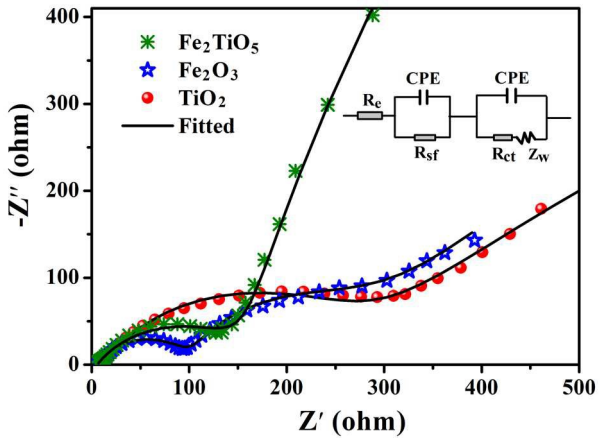

Fig. 9 Experimental and fitted Nyquist plots of TiO_2 microspheres, Fe_2O_3 nanoparticles and Fe_2TiO_5 microparticulates after 100 cycles at the current density of 100 mAh g^{-1}. The inset is the corresponding equivalent circuit.

Table of Content Entry

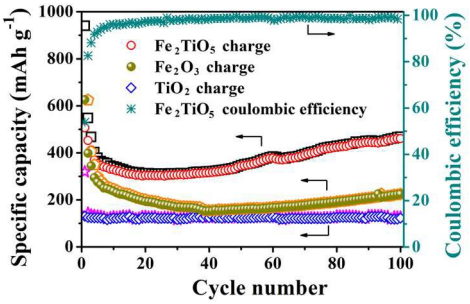

Porous Fe_2TiO_5 microparticulates exhibited superior electrochemical performances as LIBs anode material due to the synergistic effect of TiO_2 and Fe_2O_3.